SCANNING VOL. 00, 1–6 (2012)
© Wiley Periodicals, Inc.

Direct and Transmission Milling of Suspended Silicon Nitride Membranes With a Focused Helium Ion Beam

Michael M. Marshall[1], Jijin Yang[2], and Adam R. Hall[1]

[1]Joint School of Nanoscience and Nanoengineering, University of North Carolina Greensboro, Greensboro, North Carolina
[2]Carl Zeiss NTS, LLC, One Corporation Way, Peabody, Massachusetts

Summary: Helium ion milling of suspended silicon nitride thin films is explored. Milled squares patterned by scanning helium ion microscope are subsequently investigated by atomic force microscopy and the relation between ion dose and milling depth is measured for both the direct (side of ion incidence) and transmission (side opposite to ion incidence) regimes. We find that direct-milling depth varies linearly with beam dose while transmission-milling depth varies with the square of the beam dose, resulting in a straightforward method of controlling local film thickness. SCANNING 00: 1–6, 2012. © 2012 Wiley Periodicals, Inc.

Key words: helium ion microscope (HIM), atomic force microscope (AFM), ion milling, membrane, thinning

Introduction

The helium ion microscope (HIM) is a promising young technology for high-resolution imaging (Morgan *et al.*, 2006; Scipioni *et al.*, 2008; Ramachandra *et al.*, 2009). This instrument uses an atomically defined metal source to produce a coherent helium (He) beam with high brightness and small probe size. Through advanced charged particle optics and exploitation of the small de Broglie wavelength of He ions, the HIM is able to achieve a resolution of less than 0.5 nm. Furthermore, due to the slow accumulation of charge caused by the scanning He beam, the HIM has found favor as a means by which to image poorly conducting samples, including uncoated biological material (Scipioni *et al.*, 2009; Bazou *et al.*, 2011). Similar to other charged ion beam tools, the HIM can also be used for lithographically defined milling of material. Recent work has shown this capability in various materials including gold (Scipioni *et al.*, 2010), graphene (Bell *et al.*, 2009; Lemme *et al.*, 2009), and silicon nitride (Yang *et al.*, 2011), demonstrating a high level of control and precision compared to Ga-based focused ion beam (FIB) systems. This stems from the small mass of He relative to Ga, which results in reduced momentum transfer from the ion beam to the target material in the former case and thus a more regulated milling process.

A potential application of this milling control is local thickness manipulation of free-standing membranes. Ion milling is frequently used to create electron-transparent samples for transmission electron microscope imaging (Ishitani *et al.*, '94), but this preparation technique typically only needs to reach thicknesses of approximately 100 nm. Here, deep trenches are milled on either side of a small region of a substrate to achieve a thin cross-section. The HIM provides sufficient control over incident ion dose to reduce self-supported films down to small dimensions through milling in a direction perpendicular to their surface. This capability could have utility in several device architectures in which local thickness is important. For example, solid state nanopores in ultrathin membranes were recently used to detect very short biological molecules with high accuracy (Wanunu *et al.*, 2010). Accurate thickness control depends on an elucidation of both direct and transmission milling. In this work, we investigate these aspects of thin film milling experimentally.

Contract grant sponsor: North Carolina Biotechnology Center through Biotechnology Research; Contract grant number: 2011-BRG-1201.

Address for reprints: Adam R. Hall, Joint School of Nanoscience and Nanoengineering, University of North Carolina Greensboro, 2901 E. Lee St. Ste 2200, Greensboro, NC 27401
E-mail: adam.hall@uncg.edu

Received 20 August 2011; Accepted with revision 20 October 2011

DOI 10.1002/sca.21003
Published online 00 XXXX 2011 in Wiley Online Library (wileyonlinelibrary.com)

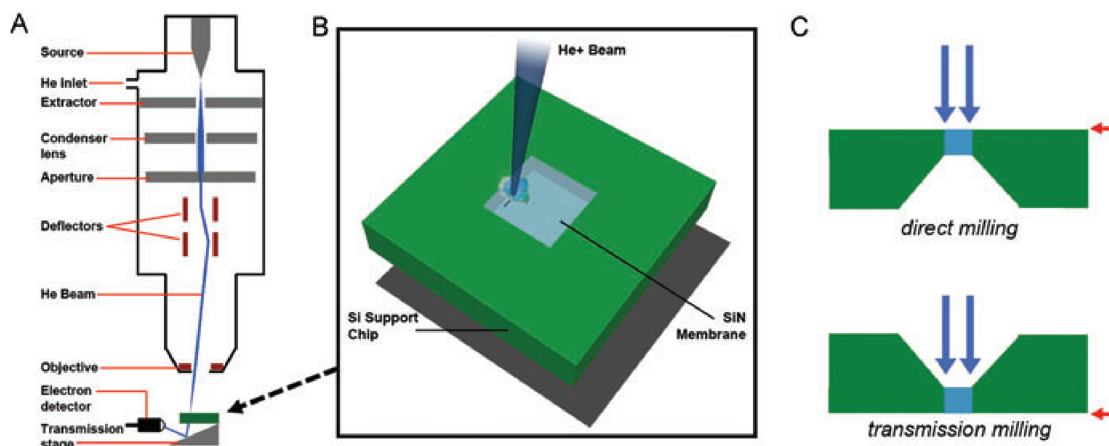

Fig 1. Experimental setup. (**A**) Schematic representation of the scanning helium ion microscope, demonstrating transmission mode imaging. (**B**) Pattern-based helium beam milling of a silicon nitride membrane supported by a silicon chip. (**C**) Schematic representations of sample chip cross-section for both direct and transmission milling (top and bottom, respectively). Blue arrows indicate milling direction and red arrows indicate the post-processing imaging surface.

Experimental Methods

Silicon chips, each supporting a single, free-standing, low-stress SiN membrane, were obtained commercially (Protochips, Raleigh, NC). Atomic force microscopy (AFM) measurements on a broken membrane yielded a film thickness of 105 nm, in agreement with the 100-nm target thickness from the manufacturer. In preparation for fabrication, a single chip was cleaned with acetone followed by ethanol and dried under nitrogen flow. The chip was then loaded into a custom transmission sample holder, the entirety of which was subsequently treated with oxygen plasma (100 W) for 5 min and introduced directly into the sample exchange chamber of a Carl Zeiss Orion Plus HIM. Here, an additional treatment of air plasma (10 W, 3 min) was used to ensure minimal contamination of the sample surface before loading the holder into the main chamber of the HIM (Fig. 1).

After insertion, the ion beam was unblanked and its current was set to a target value of 5 pA (typical accelerating voltage 30–35 kV) through a 10-μm aperture by adjusting the condenser lens setting and the He pressure. Directly prior to milling at the free-standing SiN membrane, beam shape was optimized at a nearby location on the supporting chip. Because the cleaned substrate surface was nominally featureless, a single-spot exposure (approximately 10 s) with the He beam was used to mill a structure with which to correct focus and stigmation. Once satisfactorily adjusted, the beam was blanked and the sample was moved such that the SiN window is in the beam path. There, computer control was used to unblank the beam and expose a single square (500 $\times$ 500 nm) with a set ion dose (Fig. 1B). Direct milling was performed on sample chips with the membrane side up (Fig. 1C, top). Additional squares were milled after moving the membrane a relative lateral distance of 2–4 μm in order to minimize the effects of surface charge accumulation on the milling process. Completed patterns were inspected *in situ* through transmission imaging (Fig. 2A), in which secondary electrons were recorded from an angled metal surface below the thin SiN membrane (see Fig. 1A, bottom). The increase in measured brightness at successively higher incident ion dose (Fig. 2A, bottom) indicates a greater amount of transmitted ions and thus a thinner remaining membrane thickness within the pattern.

Transmission milling is investigated by mounting a membrane-supporting chip with the membrane side down in the sample holder (Fig. 1C, bottom). The same milling procedure as detailed above is performed, resulting in the top (flat) surface of the substrate being the side opposite to the incident ion beam. This allows for direct access for subsequent AFM imaging.

Following the milling procedure, the sample is removed from the HIM and tapping mode topography images of each milled square are collected using an Agilent 5600LS AFM (Agilent Technologies, Santa Clara, CA). For these images, we use NanoWorld Arrow noncontact tips with a typical radius of curvature of $<$10 nm at the tip. The 500-nm width of the square milling patterns allows for the AFM tip to reach the bottom of the trench in all instances.

Results

A typical AFM image of four squares milled in a SiN membrane is shown in Figure 2B. This image is taken from the direct-milling side and shows the

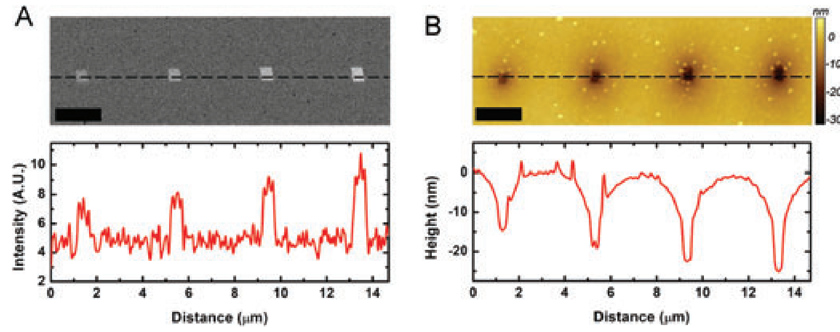

Fig 2. Images of ion-milled patterns. (**A**) Transmission HIM image of four helium beam-thinned squares (500 × 500 nm) in a silicon nitride membrane (top) and brightness profile of the image measured across the dashed line (bottom). (**B**) AFM image taken on the direct-milling side of the same four squares (top) and the height profile measured across the dashed line (bottom). In both images, the incident ion doses are 7.6×10^4, 11.4×10^4, 13.7×10^4, and 19.3×10^4 ions/nm^2 (L-R). Scale bars represent 2 μm.

same four patterns as in Figure 2A. The successively higher incident ion dose from left to right results in increasingly deeper trenches within the confines of the patterns. A topographical measurement across these images (Fig. 2B, bottom) confirms this.

The surface contour surrounding the HIM milled patterns on each side is noteworthy. On the direct-milled side, we find a gradual depression beginning 1–2 μm away from the pattern edge (Fig. 3A). Meanwhile, on the transmission-milled side, we find a volcano-like structure that surrounds the milled region and gradually declines over a distance of 1–2 μm, with its peak at the pattern edge (Fig. 3B). Similarly shaped surfaces have been observed during the closing of prefabricated apertures with a defocused ion beam (Mitsui *et al.*, 2006), where the structures were attributed to accretion of redeposited matter over long ranges due to electric field effects. This seems to be an unlikely explanation in the present experiments, however, where the additional matter is found only on the transmission side of the membrane. On the side of ion incidence, where the electric field is presumably strongest, we observe the inverse shape. Therefore, we speculate that the topographies of the membrane surfaces surrounding the milling pattern are due to a combination of charge-induced fluidization of the material, as has been documented with an electron beam (Storm *et al.*, 2003), and ion pressure. A systematic study of these effects may be useful in confirming this assertion. Nonetheless, AFM data of milled membranes and knowledge of the initial membrane thickness allow cross-sectional information to be produced. Figure 3C shows three examples of such cross-sections at average doses of (left to right) 3.9×10^4, 11.7×10^4, and 19.4×10^4 ions/nm^2, respectively. The increasing localized thinning of the membrane with dose is apparent. Interestingly, the lateral size of the exposed area on the transmission side appears slightly smaller than that of the direct side. This may be attributable to complex charging effects, which are difficult to predict.

Analysis of milling depth over a range of incident ion doses for the direct-milled side yields a clear linear dependence (Fig. 4A). This is in qualitative agreement with experimental (Tseng, 2005; Dai *et al.*, 2008) and theoretical (Behrisch, ’81; Tseng, 2004) findings. A similar analysis of the transmission-milled side yields a dependence that fits well with the square of the ion dose instead (Fig. 4B). The shape of this dependence, while qualitatively similar to previous experimental measurements (Bay *et al.*, ’76a) of transmission milling of thin films with ions, is unexpected for our experimental conditions. We discuss this further below.

Discussion

On the direct-milling side, our measurements reveal a constant material removal rate of 1.5×10^{-3} nm^3/ion. Using a density of 3.44 g/cm^3 and a molecular mass of 140.28 g/mol for silicon nitride, these data lead to a sputtering yield, S, of 0.02 atoms/ion. For comparison, we performed TRIM calculations (not shown) using values from our system: 34 keV He beam energy and 105-nm SiN membrane thickness. The resultant model yielded a value for S of 0.07 atoms/ion, in reasonable agreement with our experimental findings. Possible contributions to the slight disparity include the effects of local heating and of poor charge dissipation, both of which could impact atomic ejection efficiency but are not accounted for in modeling.

For transmission milling, an explanation for the parabolic dependence of milling depth on ion dose is not readily apparent. The origin of the behavior may be in the continual reduction in membrane thickness during the milling process, as measurements of transmission milling in other films have shown a qualitatively similar increase in yield S as membrane thickness is reduced (Bay *et al.*, ’76a,b). However, in these cases, S was shown to decrease for mem-

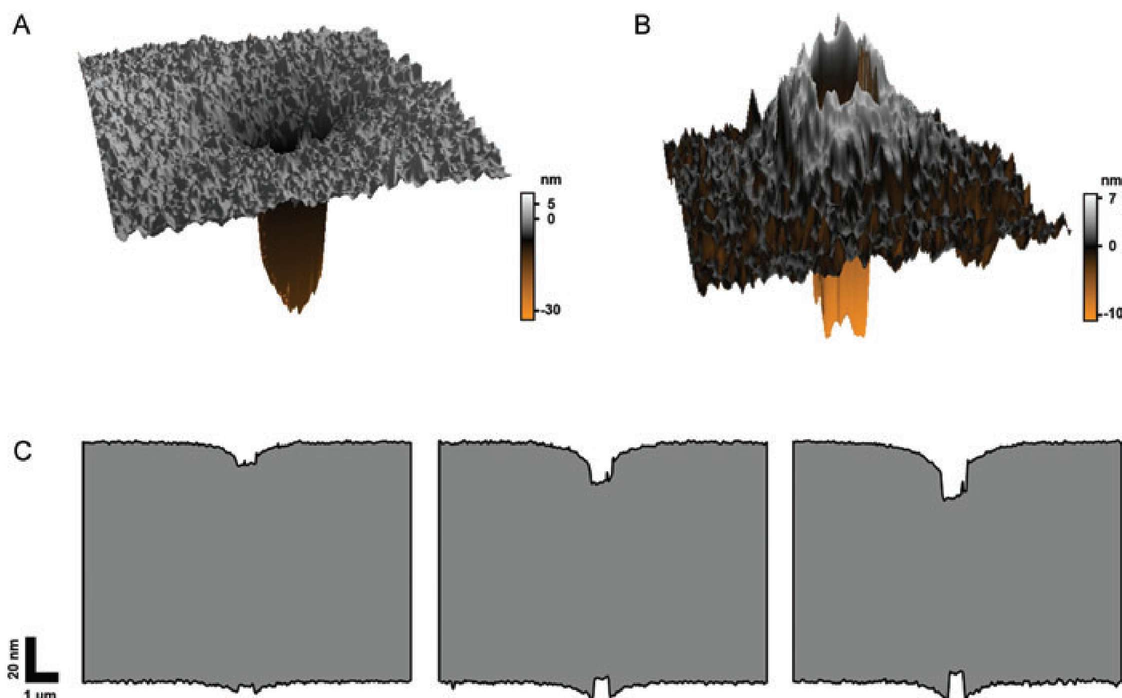

Fig 3. Topographical measurements of direct- and transmission-milled surfaces. Three-dimensional representation (3×3 μm) of AFM topography measurements on the direct- (**A**) and transmission- milled (**B**) side of a SiN membrane. Average He dose is 19.4 × 10^4 ions/nm^2. Note that both the direct- and transmission-milled surfaces face upwards for clarity. (**C**) Cross-sectional profiles of SiN membranes with 500-nm squares milled in them, reconstructed from AFM measurements of both the top and bottom surfaces. Doses are 3.9 × 10^4 (left), 11.7 × 10^4 (middle), and 19.4 × 10^4 (right) ions/nm^2.

brane thickness below the mean projected range of the ions. TRIM modeling of SiN (not shown) yields a mean projected range of 200 nm for 34 keV He ions, indicating that our initial membrane (105 nm) should already be in the regime where transmission-milling yield decreases with reducing thickness. This is counter to our experimental results. It is possible that increasing membrane fluidization lowers the energy barrier for atoms to be sputtered, but this is difficult to predict and may be expected to be measurable in direct milling as well. A possible explanation for the transmission-milling dependence observed may be direct momentum transfer from nonscattered ions at the transmission surface, the average number of which will increase with reducing membrane thickness. Additional experiments and modeling will be necessary to better understand the overall milling phenomenon in this regime.

With knowledge of the original membrane thickness, the fits to our measurements of direct- and transmission-milled depths amount to a determination of the remaining thickness inside the milled pattern for any given ion dose. Figure 4C shows this relation (solid line) in comparison with the remaining thickness dependence if only direct milling is considered (dashed line). The increasing importance of transmission milling at small membrane thickness is evident. Importantly, this assumes constant milling rates down to zero thickness. Considering that ion milling is thought to result from a cascade of atomic interactions within the bulk of the target material (Behrisch, ’81), this may not be true; as dimensions decrease, there are fewer atoms to interact with one another and thus the rate of milling may be expected to change. This may cause some deviations at very small thickness; however, the delicate nature of such thin free-standing membranes makes AFM measurements challenging. It is unknown where a divergence from the continuous relation shown in Figure 4C should be expected, partially because milling in such thin films is not fully understood.

Conclusions

We have demonstrated that the beam of a HIM can be used to control the thickness of a free-standing silicon nitride membrane. From topographical data obtained with AFM on both the side of ion beam incidence (direct milling) and the opposite side (transmission milling), we were able to reconstruct the complete profiles of milled membranes. We found that the surface surrounding the milling pattern was depressed on the direct side and enhanced on the transmission side, leading us to speculate that fluidization and ion pressure affect the surface immediately adjacent to the

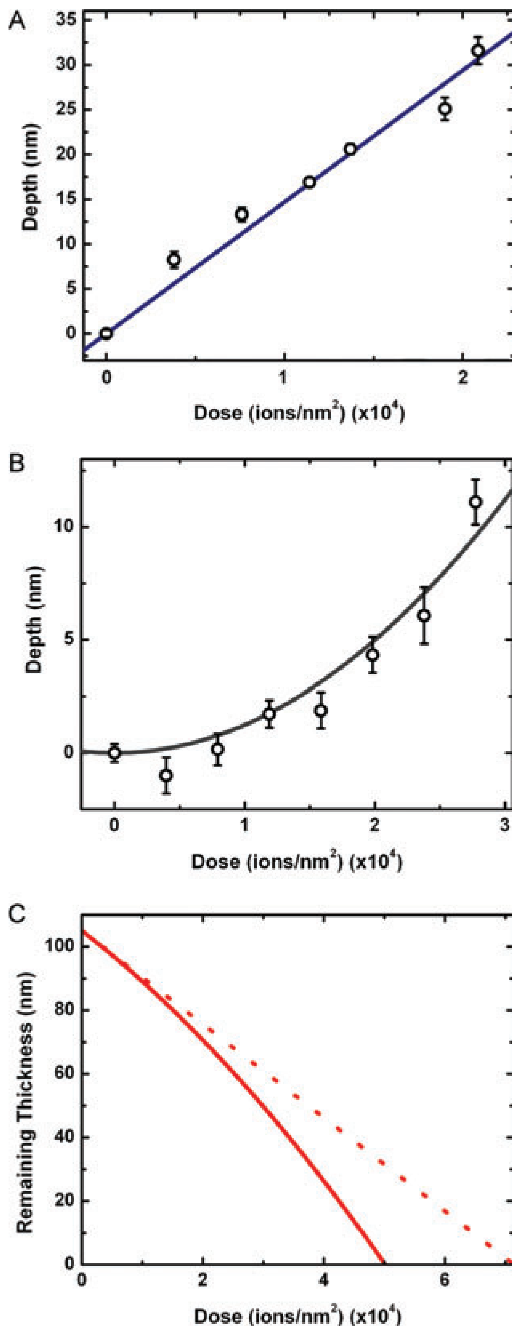

Fig 4. Ion milling depth analysis. AFM measured depths of direct-milled (**A**) and transmission-milled (**B**) squares (500 × 500 nm) in a 105-nm-thick SiN membrane for different He doses. The blue line in (**A**) and the gray line in (**B**) are linear and parabolic fits to the data, respectively. (**C**) Projected remaining thickness of a 105-nm-thick SiN membrane after exposure to the indicated He ion total dose, based on fits from (**A**) and (**B**) (solid line). Dashed line shows remaining thickness based on direct milling only.

patterned areas. By measuring milled depth relative to the unmodified membrane, we were able to quantify the material removal rate on both sides of the membrane during ion beam exposure, finding a linear relationship with dose in direct milling, and a dependence on the square of the dose in transmission milling. This resulted in an extrapolated relationship between the total ion dose and the remaining membrane thickness. This finding can be used to predict the remaining thickness of a membrane for a given dose of incident ions. We expect this technique will be useful in various applications, such as plasmonic devices (Genet and Ebbesen 2007; Scipioni *et al.*, 2010), graphene patterning (Bell *et al.*, 2009; Lemme *et al.*, 2009), and one-step fabrication of solid-state nanopores (Yang *et al.*, 2011) in ultrathin membranes.

Acknowledgements

TRIM calculations were performed using software written by J. Ziegler (http://www.srim.org). We thank S. Iyer for ellipsometry measurements of membrane thickness.

References

Bay HL, Andersen HH, Hofer WO. 1976a. Transmission sputtering as a technique for measuring distribution of energy deposited in solids by ion-bombardment. Radiat Eff Defects S 28:87–95.

Bay HL, Andersen HH, Hofer WO, Nielsen O. 1976b. Transmission sputtering yields of gold at 6.8 MeV. Appl Phys 11:289–293.

Bazou D, Behan G, Reid C, Boland JJ, Zhang HZ. 2011. Imaging of human colon cancer cells using He-ion scanning microscopy. J Micros 242:290–294.

Behrisch R. 1981. Sputtering by Particle Bombardment I: Physical Sputtering of Single-Element Solids. Springer-Verlag, Berlin.

Bell DC, Lemme MC, Stern LA, Williams JR, Marcus CM. 2009. Precision cutting and patterning of graphene with helium ions. Nanotechnology 20:455301–455305.

Dai T, Kang X, Zhang B, Xu J, Bao K, et al. 2008. Study and formation of 2D microstructures of sapphire by focused ion beam milling. Microelectron Eng 85:640–645.

Genet C, Ebbesen TW. 2007. Light in tiny holes. Nature 445:39–46.

Ishitani T, Tsuboi H, Yaguchi T, Koike H. 1994. Transmission electron-microsocope sample preparation using a focused ion-beam. J Electron Microsc 43:322–326.

Lemme MC, Bell DC, Williams JR, Stern LA, Baugher BWH, et al. 2009. Etching of graphene devices with a helium ion beam. Acs Nano 3:2674–2676.

Mitsui T, Stein D, Kim YR, Hoogerheide D, Golovchenko JA. 2006. Nanoscale volcanoes: Accretion of matter at ion-sculpted nanopores. Phys Rev Lett 96:036102–036105.

Morgan J, Notte J, Hill R, Ward B. 2006. An introduction to the helium ion microscope. Microscopy Today 14:24–31.

Ramachandra R, Griffin B, Joy D. 2009. A model of secondary electron imaging in the helium ion scanning microscope. Ultramicroscopy 109:748–757.

Scipioni L, Alkemade P, Sidorkin V, Chen P, Maas D, et al. 2009. The helium ion microscope: Advances in technology and applications. Am Lab 41:26–28.

Scipioni L, Ferranti DC, Smentkowski VS, Potyrailo RA. 2010. Fabrication and initial characterization of ultrahigh aspect ratio vias in gold using the helium ion microscope. J Vac Sci Technol B 28:C6P18–C6P23.

Scipioni L, Stern LA, Notte J, Sijbrandij S, Griffin B. 2008. Helium ion microscope. Adv Mater Processes 166:27–30.

Storm AJ, Chen JH, Ling XS, Zandbergen HW, Dekker C. 2003. Fabrication of solid-state nanopores with single-nanometre precision. Nature Mater 2:537–540.

Tseng AA. 2004. Recent developments in micromilling using focused ion beam technology. J Micromech Microeng 14:R15–R34.

Tseng AA. 2005. Recent developments in nanofabrication using focused ion beams. Small 1:924–939.

Wanunu M, Dadosh T, Ray V, Jin J, McReynolds L, et al. 2010. Rapid electronic detection of probe-specific microRNAs using thin nanopore sensors. Nature Nanotech 5:807–814.

Yang J, Ferranti DC, Stern LA, Sanford CA, Huang J, et al. 2011. Rapid and precise scanning helium ion microscope milling of solid-state nanopores for biomolecule detection. Nanotechnology 22:285310–285315.